JOURNAL OF GEOPHYSICAL RESEARCH, VOL. ???, XXXX, DOI:10.1002/,

An Euler-Lagrange approach to model local scour and sand transport

Yaru Li,[1] David M. Kelly,[2] Ming Li,[1] John M. Harris[2], and Justin R. Finn[1]

Corresponding author: Ming Li, School of Engineering, the University of Liverpool, Brodie Tower, Brownlow Street, Liverpool, L69 3GQ, UK. (M.Li@liverpool.ac.uk)

[1]School of Engineering, the University of Liverpool, Liverpool, UK.

[2]HR Wallingford, Wallingford, Oxfordshire, UK.

Abstract.

Numerical modeling of scour around offshore structures is still a challenging research topic for engineers and scientists due to the complex flow-structure-seabed interactions. In comparison to single-phase models, a multiphase approach has advantages in interpreting the flow-particle interaction, particle-particle interaction and flow-structure interaction. In the present study, an Euler-Lagrange multiphase approach is adopted to develop a new scour model in order to simulate the air-water-sediment three-phase interplay simultaneously while being computationally efficient. The model is able to represent free-surface flow over a mobile bed, which is often critical for realistic scour modeling. Based on the open source CFD software package OpenFOAM®, the model solves the Navier-Stokes equations on an Eulerian computational gird. The sediment particles are traced using the multiphase particle-in-cell (MP-PIC) method in a Lagrangian approach. The flow and sediment particles are fully coupled, and particle-particle interaction is also resolved in the model. The model is calibrated using several tests, including a falling particle and steady flow passing isolated blocks, to identify optimal parameters for model operation. Application of the model against laboratory experiments on scour development beneath a horizontal pipeline shows that the tunnel erosion stage is captured well by the model and the resolved flow structures have a dominant role in determining the shape of the eroded bed.

1. Introduction

Scour is used to distinguish the process caused by the presence of a structure from the more general term "erosion" [*Sumer and Fredsøe*, 2002]. It has long been recognized as a severe engineering safety hazard to the structures constructed in the fluvial and marine environment. In particular, large scale offshore wind farms (OWF) are being widely built at an unprecedented speed for the generation of renewable energies in the recent decades. Monopiles are the most widely adopted foundation type for OWFs nowadays. These large diameter monopiles are subject to scour in the offshore area [*Prendergast et al.*, 2015]. The scour depth can be as large as 1.38 times the monopile diameter [*Whitehouse et al.*, 2011]. At some sites where scour protections are installed, the edge scour or secondary scour around the protection can cause even deeper scour than the unprotected ones [*Whitehouse et al.*, 2011]. Therefore, it is still a challenging and urgent task to better understand the scour process and develop better prediction tools to minimize the risks associated with scour around the offshore structures like OWF foundations.

Numerical modeling of local scour around offshore structures has started with single-phase models. Works based on the potential flow theory were carried out at the early stage [*Mao*, 1986; *Li and Cheng*, 1999, 2000]. However, with the many assumptions and ad-hoc parameterizations, these models often fail to produce the whole picture of the sediment transport and scour process; only certain aspects of the problem, such as scour depth at the upstream side, can be predicted reasonably. Compared to single-phase models, the multiphase approach is gaining in popularity lately due to its capability to better interpret the flow-sediment and sediment-sediment interactions. According to the treatment

for each phase (fluid phase and solid phase), one of the following methods are usually employed: Euler-Euler methods, Euler-Lagrange methods and Lagrangian methods. In Euler-Euler models, both the fluid phase and the solid phase are regarded as continuum, and the governing equations of both phases can be solved relatively straightforwardly on an Eulerian grid. However, the fluid-particle interactions cannot be resolved naturally due to the continuum assumption of the solid phase, thus, they must be addressed explicitly with parameterizations. Moreover, Eulerian models are typically based on cell-averaged quantities, therefore, they often struggle to model complex deformation and interface fragmentation. *Zhao and Fernando* [2007] simulated the scour around pipelines using an Euler-Euler coupled two-phase model embedded in the FLUENT software, excluding the free surface effect. The inadequacy of parameterizations concerning the particle-flow interaction was found to be a major problem in their model, and it caused unrealistic particle pile-up around the pipeline. Moreover, the flow adjustment to the updated bed profile happened on a time scale which a fluid parcel took to travel the whole computational domain. This time delay made it extremely difficult for scour simulation. Besides, an initially sinusoidal bed profile had to be introduced as a disturbance to the initial evolvement of the bed. *Yeganeh-Bakhtiary et al.* [2011] developed a Euler-Euler two-phase model to simulate the tunnel erosion beneath a marine pipeline. In their model, the two-dimensional Reynolds-Averaged-Navier-Stokes (RANS) equations were solved, therefore three-dimensional features both in the hydrodynamics and scour process cannot be fully resolved. The coupling between the solid phase and the fluid phase was achieved through the drag force and lift force. However, the fluid phase and bed sediment motion was simulated separately, causing potential time delay and therefore inaccuracy in the phase

interactions. The depth of scour hole at the downstream half of the pipeline was over-predicted, and discrepancies were also observed in the bed elevation further downstream of the pipeline. Moreover, in such two-phase models, the free surface effect cannot be resolved, which limits the application of such models to scour induced by flow with limited free surface effects. Such inadequacies were also reflected in other Euler-Euler two-phase models [*Zhu et al.*, 2013].

In contrast, in Lagrangian models, such as the Smoothed Particle Hydrodynamics method (SPH) and the Moving Particle Semi-implicit method (MPS), the inherent discrete-particle property of sediment is well represented. However, as the most well-known drawback, Lagrangian models are particularly demanding on computational resources. Besides, the incorrect pressure approximation caused by a spurious pressure fluctuation is a common problem associated with the sharp fluid interfaces in such models. Therefore, either extra numerical treatment must be introduced or artificial damping factors like filtering or averaging techniques have to be involved for approximation. Moreover, in Lagrangian models, as the computational domain is discretized into particles, the representation of structures and the associated boundary condition issues are also very challenging. *Zanganeh et al.* [2012] developed a Lagrangian coupling two-phase model to study the current-induced scour. In addition to the aforementioned difficulties, in their model, the fluid phase was solved without fluid-solid phase interaction first, then it was solved again after evaluating the interphase term, and this process continued until it converged. In addition to the extra computational costs arising from such iterations, the convergence scheme also needs careful examination.

Drawing on the advantages of these two types of models, Euler-Lagrange type models provide an attractive alternative. In such models, the fluid phase is treated as continuum on an Eulerian grid, and the solid phase is treated as discrete particles. Therefore, the inherent properties of each phase are well represented, and the interaction between the phases can be resolved straightforwardly. It is also computationally efficient compared to Lagrangian models. Euler-Lagrange models have been applied to sediment transport and scour studies recently, and they have been seen as a powerful tool to resolve the physics and reveal the mechanics involved in those processes. *Yeganeh-Bakhtiary et al.* [2013] employed an Euler-Lagrange two-phase model to simulate the live bed scour beneath a marine pipeline. The Reynolds-Averaged Navier-Stokes equations was solved for the fluid phase, and the distinct element method (DEM) was employed for the solid phase. It demonstrated the model's capacity to deal with live bed scour situations, however the scour depth was under-predicted, and discrepancies were observed in the shape of the scour hole beneath the pipeline. *Andrews and O'Rourke* [1996] developed the multiphase particle-in-cell (MP-PIC) method for dense particulate flows, drawing upon the advantages of Eulerian continuum models and Lagrangian discrete models. It has been successfully applied to combustion, sedimentations, bubbling bed dynamics and many other particulate flows [*Andrews and O'Rourke*, 1996; *Snider et al.*, 1998; *Karimipour and Pugsley*, 2012; *Solnordal et al.*, 2015], which demonstrated its capacity to deal with particulate flows ranging from dilute to dense, and its advantage to reveal the physics involved in those processes. However, to the best knowledge of the authors at the time of writing, this approach has not yet been applied to scour studies. A number of challenges involved in this method hindered such applications, for example, how to incorporate the

free surface effect with the particle based approach, and how to deal with the sediment dynamics in a packed bed where the concentration is very close to fully packed conditions. With the motivation to tackle these challenges and reveal the physics involved in scouring process in the marine environment for better scour prediction, a new three-dimensional (3D) Euler-Lagrange scour model based on the MP-PIC method is therefore developed. In this paper, the theories involved in this new scour model will be presented in Section 2. Then the model is calibrated through particle falling tests, and isolated block tests. The impact of steady current on the scour development beneath a horizontal pipeline are investigated in detail. These results are presented in Section 3. The discussions and conclusions are presented in Section 4.

2. The Numerical Model

The scour model proposed here is based on the open source CFD software package OpenFOAM®[*Rusche*, 2002]. It is designed as a full three-phase model for free-surface flow over a mobile bed. The fluid phase comprises the water and air phase, and the solid phase refers to the sediment particles. The Volume of Fluid (VOF) method is employed to represent the fluid mixture and resolve the water-air interface. The modified Navier-Stokes equations are solved for the water-air mixture in the Eulerian regime based on an existing solver in OpenFOAM®. The motion of solid phase is described using the multiphase particle-in-cell (MP-PIC) method in a Lagrangian approach following Newton's Law of Motion. It is usually called two-way coupling when particle-fluid interaction is realized, and four-way coupling when particle-particle interaction is also implemented. In this model, the fluid phase and solid phase are fully coupled through the interphase momentum

transfer term. The particle-particle interaction is also represented in the particle module, therefore, the four-way coupling is achieved.

As there are a large number of particles involved in scour process, it is essential to introduce the concept of parcel, which is assumed to be a group of particles with the same properties such as size, velocity and etc. In this hybrid Eulerian-Lagrangian technique, parcels are the actual computational units in the Lagrangian framework such as to reduce the computational expense.

In this section, the governing equations for hydrodynamic module are presented first in Section 2.1. The details of the particle module are given in Section 2.2, as well as its coupling with the hydrodynamic module. The boundary and initial conditions are described in Section 2.3. The solution procedures are presented in Section 2.4.

2.1. Hydrodynamic Module

2.1.1. Governing Equation

The fluid phase, i.e., the mixture of water and air, is resolved by the incompressible Navier-Stokes equations, which are modified under the guidance of the two-fluid methodology following the work by *Rusche* [2002]. The VOF method [*Hirt and Nichols*, 1981] is employed to resolve the free surface. The governing equations are written as,

$$\nabla \cdot \mathbf{U} = 0, \tag{1}$$

$$\frac{\partial \rho \mathbf{U}}{\partial t} + \nabla \cdot (\rho \mathbf{U}\mathbf{U}) - \nabla \cdot (\mu \nabla \mathbf{U}) - (\nabla \mathbf{U}) \cdot \nabla \mu = -\nabla p_d - \mathbf{g} \cdot \mathbf{x} \nabla \rho + \sigma_\kappa \nabla \alpha + \mathbf{S}_{imt}. \tag{2}$$

where $\mathbf{U}$ is the flow velocity vector; ρ is the density; μ is the dynamic viscosity; p_d is the dynamic pressure, where the total pressure $p = p_d + \rho \mathbf{g} \cdot \mathbf{x}$, therefore, the hydro-

static component balances out the gravity force; $\mathbf{g}$ is the gravitational acceleration; $\mathbf{x}$ is the position vector; $\mathbf{S}_{imt}$ is the interphase momentum transfer term, accounting for the influence of the solid phase on the fluid phase, which will be discussed later in Section 2.2; and σ_κ is the mean curvature of the free surface given by,

$$\sigma_\kappa = -\sigma \cdot \nabla \cdot \left(\frac{\nabla \alpha}{|\nabla \alpha|}\right), \tag{3}$$

where σ is the surface tension coefficient given as a constant. α is the newly introduced phase volume fraction by the VOF method. It represents the volume fraction occupied by water within a cell. Therefore, by definition, the volume fraction occupied by air in a cell is $(1-\alpha)$. With the aid of α, the properties of the fluid phase can be expressed clearly, for example, the flow density, velocity and viscosity can be expressed in an ensemble form,

$$\rho = \alpha\rho_w + (1-\alpha)\rho_a, \tag{4}$$

$$\mathbf{U} = \alpha\mathbf{U}_w + (1-\alpha)\mathbf{U}_a, \tag{5}$$

$$\mu = \alpha\rho_w\nu_w + (1-\alpha)\rho_a\nu_a, \tag{6}$$

where the subscripts w and a represent the properties of water and air, respectively; and ν is the kinetic viscosity. It can be easily seen that in the cells full of water, the ensemble density is purely the density of water as $\alpha = 1$; and in the air, the ensemble density is purely that of air. Apparently, the ensemble velocity and viscosity follow the same rule. In these areas, the governing equations for the two-fluid methodology are purely the original Navier-Stokes equations.

The introduction of volume fraction α spontaneously requires an additional equation for α itself. The transport equation for α is given by,

$$\frac{\partial \alpha}{\partial t} + \nabla \cdot (\mathbf{U}\alpha) + \nabla \cdot [\mathbf{U}_r \alpha(1-\alpha)] = 0, \tag{7}$$

where $\mathbf{U}_r$ is the relative velocity, $\mathbf{U}_r = \mathbf{U}_w - \mathbf{U}_a$. The last term on the l.h.s. of Eq. 7 is an additional convective term, which is introduced for the purpose of achieving a higher interface resolution without using additional special convection schemes [*Jasak*, 1996]. It is noteworthy that this term is applicable only within the interface region, of which the thickness is theoretically infinitesimal. With the definition of α itself, this term vanishes in cells where there is purely water or purely air.

The Finite Volume Method (FVM) is employed to discretize the Eulerian solution domain into control volumes (CV) (see Figure 1), which are also called cells. $\mathbf{x}_{i,j,k}$ is the position vector of the cell center, $V_{i,j,k}$ is the cell volume, and $\mathbf{S}$ is the face area vector, normal to the face and pointing outward of the cell. These control volumes are arbitrarily unstructured; therefore it is convenient to resolve complex geometry and achieve local grid refinement. More details can be found in *Jasak* [1996].

2.1.2. Turbulence Model

The standard turbulence models available in OpenFOAM® includes Reynolds-Averaged models such as $k-\varepsilon$ model and $k-\omega$ model, and large eddy simulation (LES) such as the $k-$equation sub-grid-scale models [*A.*, 1993]. The transport equation for sub-grid-scale kinetic energy k_{sgs} can be written as,

$$\frac{\partial k_{sgs}}{\partial t} + \frac{\partial (u_j k_{sgs})}{\partial x_j} = \frac{\partial}{\partial x_j}[(\nu + \nu_{sgs})\frac{\partial k_{sgs}}{\partial x_j}] - C_\varepsilon \frac{k_{sgs}^{3/2}}{\Delta} + 2\nu_{sgs}\mathbf{S}_{ij}\mathbf{S}_{ij}, \tag{8}$$

where the sub-grid-scale eddy viscosity $\nu_{sgs} = C_k k_{sgs}^{1/2}\Delta$, Δ is the cell length scale, and $\mathbf{S}_{ij}$ is the strain tensor rate, and C_ε and C_k are constant.

2.2. Particle Module

In the hydrodynamic module, all the dependent variables of the fluid phase are associated with and solved on the Eulerian grid. In the particle module, the sediment particles are treated individually as discrete particles, and is solved using Newton's Law of Motion in a Lagrangian framework. The multiphase particle-in-cell (MP-PIC) method is adopted to advance the particles, which as its name suggests, particles are dealt with on a sub-grid scale. Figure 2 shows a sketch of particles within a control volume, where p_i and p_{i+1} denotes the particles, and $\mathbf{x}_{p_i}$ and $\mathbf{x}_{p_{i+1}}$ are the corresponding position vectors. In this work, the particle motion caused by the hydrodynamic drag force, the pressure gradient force, net buoyant force and the inter-particle stress are all taken into consideration. To access the flow velocity and other related parameters such as to compute the particle motion, the computed hydrodynamic variables are interpolated from the Eulerian grid to the discrete particle positions.

In the multiphase particle-in-cell method, a particle distribution function $\phi(\mathbf{x}_p, \mathbf{U}_p, \rho_p, V_p, t)$ is introduced to describe the particle concentration on the basis of the Eulerian grid. The particle distribution function follows the Liouville equation[*Snider*, 2001]:

$$\frac{\partial \phi}{\partial t} + \nabla_x \cdot (\phi \mathbf{U}_p) + \nabla_{\mathbf{U}_p} \cdot (\phi A) = 0, \tag{9}$$

where the subscript p represents the particles, V_p is the particle volume, and A is the particle acceleration, $A = \frac{d\mathbf{U}_p}{dt}$.

Following Newton's Law of Motion, the governing equation for the solid phase read,

$$\frac{d\mathbf{U}_p}{dt} = D_p(\mathbf{U}_f - \mathbf{U}_p) - \frac{\nabla p}{\rho_p} + (1 - \frac{\rho_f}{\rho_p})\mathbf{g} - \frac{1}{\theta_s \rho_p}\nabla\tau, \tag{10}$$

where the subscript p represents the particles, the subscript f represents the fluid phase, D_p is a parameter related to drag coefficient C_d, and θ_s is the solid volume fraction, which will be introduced later on. Terms on the r.h.s. account for the particle acceleration due to the hydrodynamic drag force, the pressure gradient force, the net buoyant force (gravity minus buoyant force), and the inter-particle stress gradient, respectively. As the solid phase is treated as discrete particles, no discretization scheme is needed in the Lagrangian framework.

Once the particle velocity is computed, the particle position can then be updated by

$$\frac{d\mathbf{x}_p}{dt} = \mathbf{U}_p. \tag{11}$$

As the sediment particles are evolved on a sub-grid scale using the multiphase particle-in-cell (MP-PIC) method, the particles' information within a cell will get integrated and stored as Eulerian variables, via whom the fluid phase can get the feedback from the solid phase. The solid volume fraction θ_s is an essential variable for this purpose. It accounts for the volume fraction occupied by the solid particles within a cell. The solid volume fraction in a cell is

$$\theta_s = \int\int\int \phi V_p dV_p d\rho_p d\mathbf{U}_p. \tag{12}$$

By definition, θ_s should be no greater than 1. However, in the case of sandy particles, the porosity determines that the maximum volume concentration for fully packed bed is approximately 65%. Therefore, a critical solid volume fraction θ_{cs} should be employed, and it is usually assigned around $0.6 - 0.65$.

2.2.1. Drag Model

The drag force model by *Andrews and O'Rourke* [1996] is selected in this work. The parameter D_p, the drag coefficient C_d, and particle Reynolds number Re_p in the hydrodynamic drag term read,

$$D_p = C_d \frac{3}{8} \frac{\rho_f}{\rho_p} \frac{|\mathbf{U}_f - \mathbf{U}_p|}{r_p}, \tag{13}$$

$$C_d = \frac{24}{Re_p}(\theta_f^{-2.65} + \frac{1}{6} Re_p^{2/3} \theta_f^{-1.78}), \tag{14}$$

$$Re_p = \frac{2\rho_f |\mathbf{U}_f - \mathbf{U}_p| r_p}{\mu_f}, \tag{15}$$

where r_p is the radius of the particle, θ_f is the fluid phase volume fraction, i.e., $\theta_f = 1 - \theta_s$.

2.2.2. Inter-particle Stress

When the solid volume fraction exceeds 5%, frequent particle collisions will take place [*Patankar and Joseph*, 2001]. When the particles are traced in the Lagrangian framework, it is straightforward to compute the particle collision effect on a particle-to-particle basis using Lagrangian collision models. However, with the huge number of particles involved, it will obviously consume a significant amount of computational resource to model the

particle-particle collision, which means a large amount of CPU time is required, and the Euler-Lagrange model will lose its computational efficiency. Instead, the effect of an isotropic particle collisional pressure based on the Eulerian grid is usually adopted to represent particle collisions and prevent the solid volume fraction from exceeding its critical value. Such continuum models have been proven to be suitable and efficient in Eulerian-Lagrangian models [*Patankar and Joseph*, 2001; *Snider*, 2001].

A continuum particle stress model by [*Snider*, 2001] is employed here to take into account the particle collision effect. In this model, the assumption of an isotropic inter-particle stress is made, where the off-diagonal elements of the stress tensor are omitted. The particle normal stress is modeled by a continuum calculation of the particle pressure based on the Eulerian grid, which will then be interpolated back to the discrete particle's positions to calculate the normal stress due to motion and inelastic collision of particles. The model is given by,

$$\tau = \frac{P_s \theta_s^{\beta}}{max[\theta_{cs} - \theta_s, \varepsilon(1 - \theta_s)]}, \tag{16}$$

where P_s is a constant with the unit of pressure, and the recommended value of the constant β is $2 \leq \beta \leq 5$. A small number ε of the order 10^{-7} is introduced to remove the spikes at close pack. Obviously, this model depends only on the solid volume fraction, and the particle size and velocity are excluded. However, this simple model has been applied to several dense particulate flow circumstances [*Snider*, 2001; *Patankar and Joseph*, 2001], and has been proven to be efficient.

A particle might be moving towards a fully packed cell, and the inter-particle stress model helps to suppress this particle motion and prevent the solid volume fraction from

exceeding the critical value. Practice however shows that the inter-particle friction is often significant and the inter-particle stress alone is not sufficient enough to completely prevent the cells from being fully packed, which will cause both numerical instability and physical unreality. This is due to the fact that the inter-particle stress model is simply an approximation to partly account for the particle collision effect, the rest of the particle collision effect and the particle friction are not represented. Out of technical considerations, when a particle is moving towards a fully packed region, in principle, it is forbidden. However, if the destination cell has a neighbor cell which is able to accommodate a new particle, this particle can be moved there. This is in line with the fact that when a particle enters a fully packed cell, another particle in the same cell can be repelled into a less packed region due to collision. In this way, it compensates for the friction effect and the part of collisional effect which is not reflected in the inter-particle stress model of [*Snider*, 2001].

2.2.3. Particle Tracking Method

In hybrid Eulerian-Lagrangian models, it is essential to know where the discrete Lagrangian particles are on the Eulerian grid, so that the Lagrangian particles can be influenced by the fluid phase correctly via the dependent variables on the Eulerian grid, and meantime the Lagrangian source terms can be imposed to the correct Eulerian cells. Therefore, for each and every particle, we must know the cell which possesses this particle.

The most straightforward way to achieve that is to search the whole Eulerian grid with the particle position. However, even regardless of the number of cells in the computational domain, the number of particles alone makes it extremely expensive to do the searching at every time step.

A more mature and efficient way to track the particles was proposed and revised by *Nordin* [2000] and *Macpherson and Weller* [2009]. This tracking method is adopted in this work. The cell occupancy information of all the particles is initialized only once at the beginning of simulations, and will be stored in following time steps unless being changed. For example, when a particle moves from its initial position **a** to the final position **b** at the end of this Eulerian time step dt, as depicted in Figure 3, its trajectory will intersects with Face 2 by **p** first and then the face shared by Cell B and Cell C by **p'**.

Rather than moving the particle directly to the final position **b**, the trajectory will be split into three parts: **ap**, **ap'**, and **p'b**. Consequently, the Eulerian time step will be split into three Lagrangian sub-time-steps, corresponding to each section of the trajectory. Considering the particle moving from **a** to **p**, which is right on the face, the following equations are satisfied:

$$\mathbf{p} = \mathbf{a} + \lambda_a(\mathbf{b} - \mathbf{a}), \tag{17}$$

$$(\mathbf{p} - \mathbf{C}_f) \cdot \mathbf{S} = 0, \tag{18}$$

where $\mathbf{C}_f$ is the face center, $\mathbf{S}$ is the face normal vector, and λ_a is a fraction parameter introduced to split the whole trajectory into sections. Combining these two equations, λ_a can be derived by

$$\lambda_a = \frac{(\mathbf{C}_f - \mathbf{a}) \cdot \mathbf{S}}{(\mathbf{b} - \mathbf{a}) \cdot \mathbf{S}}. \tag{19}$$

With a visualized figure we can see which faces the particle will cross, however, during computation, the model needs a criteria to determine which faces are to be crossed and

how the Lagrangian sub-time-steps are set. Taking a two-dimensional grid shown in Figure 3 as an example, a λ_a value for each face from Face 1 to Face 4 can be calculated using Eq. 19. If a face is to be crossed by the particle, the λ_a value of this face should be the lowest in the the range $0 \leq \lambda_a \leq 1$, among all the faces of the original Cell A. In Figure 3, Face 2 meets this criteria, so it will be crossed. Therefore, the particle will be moved to position **p** with the consumption of sub-time-step $\lambda_a dt$. As Face 2 is shared by Cell A and Cell B, the cell occupancy of this particle will be transferred to Cell B at this point. It saves the effort to search for the whole grid by utilising the face connectivity information. In the next sub-time-step, the same calculation procedure will be applied to determine which face of Cell B will be crossed so that it can move to position **b**. In this example, the particle will be moved from **p** to **p'** and the cell occupancy will be transferred to Cell C. Again, we calculate the λ_a value of each face in Cell C, however, none of these values comply with the aforementioned criteria; they are either greater than 1 or less than 0, which means the final destination lies in the same cell and no face will be crossed. Therefore, the particle will be advanced to the final position **b** using the remaining sub-time-step.

This method works well in the situations discussed above. However, when it comes to three-dimensional unstructured grid, with non-planar cell faces, especially in concave cells, it is not robust enough. For example, a face plane can be hit while the particle still remains in the same concave cell. When the face is hit, the cell occupancy is transferred to its neighbour cell sharing this face already, but the particle is still in the original cell physically. Thus in the next sub-time-step, the particle will get lost. To overcome this deficiency, *Macpherson and Weller* [2009] modified the method by introducing another

fraction parameter λ_c. It is calculated simply by replacing position **a** with the cell centre $\mathbf{C}_c$,

$$\lambda_c = \frac{(\mathbf{C}_f - \mathbf{C}_c) \cdot \mathbf{S}}{(\mathbf{b} - \mathbf{C}_c) \cdot \mathbf{S}}. \tag{20}$$

λ_c of each face is calculated first. If $\lambda_c < 0$ or $\lambda_c > 1$ applies to all the faces, the final destination **b** is within the same cell, so the particle will be advanced to **b** directly, and the cell occupancy remain unchanged. If $0 \leq \lambda_c \leq 1$, which means the particle will hit a face before reaching the final destination, λ_a of each face will then be calculated and the face to be hit will be determined using the aforementioned criteria. The particle will be moved to an intermediate position **p** using Eq. 17, and cell occupancy will be changed. These procedures will be repeated until the final destination **b** is reached. This modified tracking algorithm is employed in this work. More details can be found in *Macpherson and Weller* [2009].

2.2.4. Interphase Momentum Transfer

In scour process, particles roll, slide or saltate along the bed, get entrained in the flow and evolve with flow by gaining kinetic energy from the flow. In return, particles act as a momentum sink to the fluid phase. This effect is usually reflected by the interphase momentum transfer in multiphase flow.

Particles are influenced by the flow through the drag force and pressure gradient force, spontaneously particles gain the certain amount of momentum from the fluid phase and meantime the fluid phase lose the same amount. Following the work of *Snider* [2001] and *Patankar and Joseph* [2001], the momentum transfer from the solid phase acting on each cell, $\mathbf{S}_{imt}$, is summed as,

$$\mathbf{S}_{imt} = -\sum_{i=1}^{N_p} \Big[D_p(\mathbf{U}_f - \mathbf{U}_p) - \frac{1}{\rho_p}\nabla p \Big]. \tag{21}$$

2.2.5. Mixture Viscosity

In addition to the momentum transfer, the viscosity of the fluid phase is also influenced by the presence of particles. Past studies show that in dilute suspensions, concentration and viscosity are linearly related [*Einstein*, 1906; *Penko et al.*, 2009], and as the concentration approaches the maximum packing status, the viscosity becomes infinite [*Eilers*, 1941; *Penko et al.*, 2009].

Considering the Eulerian-Lagrangian framework, the Eilers equation [*Eilers*, 1941; *Penko et al.*, 2009] is employed to modify the fluid phase bulk viscosity, which reads,

$$\mu' = \mu[1 + \frac{0.5\mu_0\theta_s}{1 - \theta_s/\theta_{cs}}]^2, \tag{22}$$

where μ_0 is the intrinsic viscosity, which accounts for the shape of particles. For spherical particles, $\mu_0 = 2.5$ is recommended, and for irregularly shaped particles, the determination of μ_0 stays uncertain [*Einstein*, 1906; *Penko et al.*, 2009].

Apparently, the bulk viscosity is a function of the particle shape, the local sediment volume fraction and critical solid volume fraction. In general, the modified bulk viscosity μ' is no less than the original fluid viscosity μ. In a cell comprising water and air only, the solid volume fraction θ_s is zero, thus the bulk viscosity μ' converts back into the original viscosity of the pure fluid μ. When a cell is approaching the maximum packing status, for example, $\theta_s = 0.64$ and $\theta_{cs} = 0.65$, the modified viscosity is approximately 2800 times

the original viscosity, in line with rules discovered by the past studies [*Eilers*, 1941; *Penko et al.*, 2009].

2.3. Boundary and Initial Conditions

The two typical numerical boundary conditions, namely, the Dirichlet boundary condition and the von Neumann boundary condition, are built in the hydrodynamic module [*Jasak*, 1996]. Dirichlet boundary condition prescribes the value of dependent variables on the boundary directly, and the von Neumann boundary condition prescribes the gradient of the variables normal to the boundary. In the former case, a fixed value ϕ_B can be specified on the boundary and therefore, the values on the cell faces along this boundary are all assigned as $\phi_f = \phi_B$. In the latter case, the face gradient $\nabla\phi$ is specified, and the boundary face value can be computed by

$$\mathbf{S} \cdot \nabla\phi = |\mathbf{S}| \frac{\phi_f - \phi_P}{d_n}, \tag{23}$$

where ϕ_f and ϕ_P are the value of the variable on the boundary face and at the cell centre of this boundary cell, respectively, and d_n is the distance from the cell centre to the face, which is also normal to the face area.

The boundary conditions in the hydrodynamic module are also applicable to the solid-phase-related Eulerian variables such as solid volume fraction θ_s. For the Lagrangian variables such as particle position and particle velocity, as they are determined by Newton's Law of Motion, once the initial values are assigned, those values will be updated accordingly. When a particle reaches the downstream boundary, it will no longer remain

in the solution domain. If periodic boundary condition is assigned, particles will enter from the corresponding boundary again into the computational domain.

2.3.1. Initial Conditions

The initial conditions in the hydrodynamic module can be specified easily in the input files for each Eulerian variable according to test configurations. In the particle module, as parcels are the actual computational unit, the input files required here are the diameter, velocity and position of the parcels, therefore, the governing equation of the particles can be solved accordingly.

2.4. Solution Procedures

For the particle module, as it is already on a discrete particle-to-particle basis, the calculation is straightforward. The fluid properties on the Eulerian grid will be linearly interpolated to the particle position prior to advancing the particles.

The pressure-velocity coupling of the Navier-Stokes equations requires special treatments. The PIMPLE algorithm is employed for this purpose. It is a merged algorithm of PISO (Pressure Implicit with Splitting of Operators) [*Issa*, 1986] for transient flows and SIMPLE (semi-implicit method for pressure-linked equations) for steady flow [*Patankar*, 1981]. In these algorithms, the equations are all solved in a segregated approach. More details can be found in *Jasak* [1996].

The solution procedures are summarized here:

1. Set up the initial fields.
2. Solve the transport equation of volume fraction α.
3. Correct water and air phase properties.

4. Solve the momentum equation.

5. Enter pressure correction loop and solve the Poisson Equation until the desirable residual tolerance is reached. The conservative fluxes are also obtained at each step.

6. Solve and correct the turbulence model if applicable.

7. Advance the particles using Eq. 10 and Eq.11.

3. Results and Discussions

Prior to realistic applications, the model needs to be calibrated. In the model calibration, firstly, the particle-motion-related implementations are calibrated through particle falling tests. The computed particle fall velocity is compared to its theoretical value. Secondly, the physical influence of particles on the fluid phase achieved by the model was examined by isolated block tests. Then, the model is applied to a benchmark scour test by *Mao* [1986].

3.1. Model Calibration

3.1.1. Particle Falling Tests

Particle falling tests are carried out to examine the numerical implementation concerning particle motion. Cases with various particle median diameter $d50$ are simulated. The computed particle fall velocity is compared to its theoretical value. In addition, cases with various grid spacing ratio to parcel diameter are tested to get a desirable range of this size ratio.

Two single-parcel-falling-in-still-water tests are carried out respectively to examine the model's behavior at low solid volume fraction. The only difference between these two tests is the number of particles per parcel (see Table 1), consequently, the particle $d50$

varies. The test domain in both tests is 0.05 m long, 1 m high, and 0.005 m wide. The grid spacing is 0.005 m uniformly in each direction, therefore, the transverse direction z is one cell wide. The water depth is 0.8 m. A parcel of the diameter 2.5 mm is released from rest at 0.7 m high.

To verify the model in terms of particle motion, the modeled particle velocity is compared with the theoretical value. Following the approach of *van Rijn* [1993], the theoretical fall velocity is determined from the balance of forces on a particle (Eq. 24) with the assumption that the flow velocity is zero. The terms on the l.h.s. of Eq. 24 represent the gravitational force, the buoyant force and the drag force on the particle, respectively.

$$\frac{\pi}{6}d^3\rho_p g - \frac{\pi}{6}d^3\rho g - \frac{1}{2}C_d\rho w_s^2(\frac{\pi}{4}d^2) = 0. \tag{24}$$

Here, d is the particle diameter, ρ_p is the density of the particle, ρ is the density of water, and w_s is the particle fall velocity in a still fluid. The drag coefficient C_d in the model is expressed by Eq. 14, which is a function of the particle Reynolds Number (see Eq. 15). As the water is assumed to be still, $\mathbf{U}_f = 0$ is satisfied in Eq. 15, and $\mathbf{U}_p$ thus equals to w_s. A non-linear equation of w_s can be derived by substituting Eq.14 and Eq.15 into Eq.24, which reads,

$$C_1 w_s + C_2 w_s^{1.667} - C_3 = 0 \tag{25}$$

where C_1, C_2 and C_3 are constant:

$$C_1 = \theta_f^{-2.65} \tag{26}$$

$$C_2 = 0.1667(\frac{\rho d}{\mu})^{0.667}\theta_f^{-1.78} \quad (27)$$

$$C_3 = \frac{(\rho_p - \rho)gd^2}{18\mu} \quad (28)$$

By solving this non-linear equation, the theoretical fall velocity of $PFV-1$ and $PFV-2$ are 0.3114 $ms^{-1}$and 0.0293 ms^{-1}, respectively. To satisfy the assumption that the flow is stationary during the simulation, the influence of particles on the fluid phase was turned off in the model, therefore the fluid phase remains undisturbed.

Good agreement between the modeling results and the theoretical fall velocity is shown in Figure 4. The modeled particle fall velocity and the theoretical value in PFV-1 are 0.32 ms^{-1} and 0.3114 ms^{-1}, respectively. Those in PFV-2 are 0.029 ms^{-1} and 0.0293 ms^{-1}, respectively. The modeled discrepancy is 2.69% in $PFV-1$, and 1.02% in $PFV-2$. Considering numerical accuracy limited by truncated errors and etc., this high agreement between the modeled value and theoretical value is remarkable. It confirms that the numerical implementation in the model concerning particle motion is reliable. Figure 4 also illustrates that the initial acceleration stage differs betweent these two tests. In $PFV-1$, the particle velocity has reached its terminal velocity since around 0.18 s, whereas in $PFV-2$, the terminal velocity is obtained almost instantly after release. This demonstrates the fact that the fall velocity of fine particles is much smaller and can be reached quickly than that of the coarse ones. Through these two tests, the particle motion related implementation especially the drag force is calibrated successfully.

3.1.2. Isolated Block Tests

The physical influence of particles on the fluid phase achieved by the model, in particular, the interphase momentum transfer term, is examined by the isolated block tests in this section. These tests involve large number of particles in nearly fully packed condi-

tions. To make it simple and straightforward, an isolated block of particles is placed in the flow. Tests with the isolated block located in the middle of the flow (Test MDL), and on the bottom wall (Test BTM) are performed respectively. To minimize other effects, the bulk viscosity remains unmodified and the particles are fixed to see the reaction of the flow field to the presence of particles. Therefore, the performance of the interphase momentum transfer term can be clearly reflected.

The mesh resolution in these tests is 2.5 mm, and the transverse direction z is one cell wide. Slip boundary conditions are applied to the $xy-$planes. A steady current boundary condition is imposed on the inlet boundary. The mean flow velocity is 0.35 ms^{-1}. The diameter of the parcel is 0.72 mm, and particle $d50$ is 0.36 mm. The maximum solid volume fraction in the block is 0.58.

The modeled flow fields and velocity profiles at selected sections are shown in Figure 5. We can see that the physical effects of the interphase momentum transfer term are well represented. As shown in Figure 5-a), the flow decelerates at the upstream circumference of the block and flows around the block. As the block of particles is a porous medium, very small seepage flows are observed inside the block as expected. While flowing around the block, the flow accelerates again and a recirculation zone is formed at the lee-wake side. As seen in Figure 5-b, the flow velocity at the upstream edge of the block is almost zero, and the flow deceleration around the block, and the acceleration further above and below are clearly captured. The flow reversal and the vortices in the lee-wake side are also resolved.

To testify the performance of the interphase momentum transfer term at boundaries, the block of particles is placed on the bottom boundary (Test BTM). The flow deceleration

at the upstream of the block, the re-acceleration above the block, and the recirculation in the wake side are all captured well as shown in Figure 5-c and 5-d.

3.2. Model Application

The model is applied to the current-induced live-bed scour around a pipeline, a benchmark laboratory test carried out by *Mao* [1986]. The water depth is 0.35 m and pipeline diameter $D = 0.1\ m$. In this selected live-bed scour case, the Shields number $\theta = 0.098$ and the mean flow velocity is 0.5 ms^{-1}.

3.2.1. Flow Field and Bed Profile

The computational domain is 1.6 m long, 0.5 m deep and one cell wide. The mesh resolution is 5 mm. The $k-$equation large eddy simulation (LES) (see Eq. 8) is adopted to resolve the turbulence structures. The modeled water velocity field at $t = 1.5\ min$ is shown in Figure 6, where the bed is colored in red. By large, the flow field $1D$ above the bed at the upstream side remains undisturbed. Apart from this region, the flow field is influenced by the presence of the pipeline and sediment particles remarkably. When the flow approaches the pipeline, the flow acceleration around the pipeline is well captured. In the downstream side, the recirculation zone right behind the pipeline and two small cavities between the flow acceleration zone and the recirculation zone are all captured clearly. The lee-wake vortices are formed behind the recirculation zone. The flow field right above the bed is also resolved vigorously. At the upstream side, small vortices come into being and develop along the streamwise direction. Flow velocity right above the bed is very minor because the particles act as a momentum sink. In conjunction with the shear stress in the flow field further above the bed, those vortices are formed. At $t = 1.5$ min, the scour hole beneath the pipeline has already formed a well-shaped passway for the

flow. Therefore, the flow acceleration between the bed and the pipeline develops without much obstacles. The acceleration jet propagates to around $2D$ behind the pipeline and encounter the flow from above the pipeline. Consequently, the lee-wake vortices take place and propagate further to the downstream side. Between the lee-wake vortices and the bed, the flow is hindered by the bed, especially the mount shaped at $x = 1.8D$. Also we can see that the free surface is no longer level at the initial water depth. Due to the flow acceleration and lee-wake vortices caused by the the pipeline, the water level decreases from $x = -1D$ and fluctuates in the downstream side. By resolving the free surface, the internal flow field can adjust more realistically and timely to the bed profile evolvement.

The modeled bed profile at $t = 1.5\ min$ is compared to the measurements [*Liang et al.*, 2005] in Figure 7. The shape of the scour hole, the maximum scour depth, and the maximum deposition point in the downstream side are all in good agreement with the measurement, which is the major task of scour prediction. However, some discrepancies are observed around $x = -1D$ and in the downstream side. In the modeled result, the bed is scoured slightly deeper between $x = -0.6D$ and $x = -0.8$. That can be caused by the over-predicted vortex at this location. The over-predicted bed elevation in the downstream side can be associated with the weak flow there, which is not sufficient to wash the sediment particles further downstream. However, the overall performance of the model to resolve the local scour is satisfactory.

3.2.2. Sub-grid-scale Turbulence Structures

The couture of the sub-grid-scale kinetic energy and sub-grid-scale eddy viscosity captured by the model are shown in Figure 8. Obviously, the sub-grid-scale kinetic energy is more intense on the two sides of the pipeline as shown in Figure 8-a. The high value region

below the pipeline is even larger than that above the pipeline. Along the bed surface at the upstream side, higher values of sub-grid-scale kinetic energy than the majority water body are observed, and the high value region extends to the downstream side of the scour hole. In Figure 8-b, the high value region of sub-grid-scale eddy viscosity overlaps with the bed surface area, around the pipeline circumference, and also the recirculation zone behind the pipeline and the location of lee-wake vortices. These regions are also where particle motions are very active as will be shown in Figure 9. Therefore, the authors reckon that the implications of particle motion with respect to the sub-grid-scale kinetic energy and eddy viscosity, and even their interactions are an exciting topic to investigate. The high sub-grid-scale kinetic energy and sub-grid-scale eddy viscosity in those regions can be the drive to facilitate particle motion especially particle entrainment. However, the main flow in those regions is usually strong compared to other areas, which is also important to particle motion. One cannot say that the active particle motions there are mainly due to the sub-grid-scale turbulence structures. Nevertheless, the particles are also at a sub-grid-scale. The interactions between the particles and sub-grid-scale turbulence structures can more straightforward and vigorous.

3.2.3. Particle Evolvement

One of the advantages of this model is to trace the discrete particles in a natural way. Consequently, the sand transport can be resolved naturally, and the particle distribution and evolvement can be investigated easily. Figure 9 shows the particle distribution at selected time. The particles are colored in red, and the flow velocity vectors at every 50 points on the Eulerian grid are also plotted. In Figure 9-a, we can see at $t = 4\ s$, particles at the bed surface in the upstream side are dragged by the flow and starts rolling and

sliding along the bed. The bed between $x = -0.8D$ and $x = -0.2D$ starts to be scoured and a very mild curve forms beneath the pipeline. Compared to the upstream side, the particle motions in the downstream side is more vigorous mainly due to the complex flow structure developed there. We can see at this very beginning of scour development, a large amount of particles have been entrained into the flow, and the bed surface in the downstream side has started to deform. At $t = 12\ s$, the scour hole extends upstream to $x = -1.6D$, and the gap right beneath the pipeline is enlarged as shown in Figure 9-b. As a consequence, particles are piled up near $x = 0.8D$. As time goes on, the scour hole at the upstream side continues developing, the gap between the pipeline and the bed keeps enlarging, and the maximum scour location evolves downstream towards right beneath the pipeline (see Figure 9-c, Figure 9-d, Figure 9-e and Figure 9-f). In addition, it is shown that the scour development at the beginning is largely dominated by scattering events. As time goes on, such phenomenon weakens, and instead the scour hole gradually takes shape. It demonstrates the ability of the model to clearly reproduce the tunnel erosion stage by tracing the particles in the Lagrangian framework, and even the onset of scour can be reflected as well without using an initial artificial bed profile to facilitate scour development as seen in other models [*Liang et al.*, 2005; *Zanganeh et al.*, 2012].

3.2.4. Modified Viscosity

As introduced in the preceding paragraphs, the bulk viscosity is modified to account for the influence of particles on the fluid phase. Employing Eilers Equation (Eq. 22) [*Eilers*, 1941; *Penko et al.*, 2009], the modified viscosity largely depends on the distribution of solid volume fraction. In Figure 10-a, the distribution of the solid volume fraction is depicted. From the bed surface to the bottom, the solid volume fraction increases towards

fully packed condition. The isolines are parallel to the bed surface profile by large as expected. As seen in Figure 10-b, the distribution of the modified viscosity follows the distribution pattern of the solid volume fraction. The increase in the modified viscosity is more dramatic where the solid volume fraction exceeds 0.55, compared to the bed surface regions where the solid volume fraction is between 0.35 to 0.55. Therefore, the modified viscosity mainly serves to stabilize the bed, and it has little influence in the main water body above the bed, where the solid volume fraction is very small due to the dilute suspension.

3.2.5. Influence of Hydrodynamics on Bed Profile

Five follow-up tests are set up as shown in Table 2 to investigate the influence of the modified viscosity and turbulence models on the bed profile. The results shown above are from Test 6 with modified fluid viscosity and using LES. In comparison, Test 5 also uses LES but the fluid viscosity remains unmodified. In Test 3 and 4, the standard $k-\omega$ turbulence model is employed, either with or without modified viscosity. No turbulence model is adopted in Test 1 and 2.

The modeled bed profile and flow field in each test are shown in Figure 11 and Figure 12, respectively. In these two figures, results of Test 1 to Test 6 are shown in the sub-figure a to f in sequence. The fluid viscosity is not modified in the tests on the left column, in contrary to the modified viscosity in those on the right column. No turbulence model is used in the two tests on the top panel. On the middle panel, the $k-\omega$ turbulence model is employed; and on the bottom panel, LES is adopted. In Figure 11, we can see that the shape of the scour hole and the maximum scour depth in each test are all in good agreement with the measurements, which is the major purpose of scour prediction.

However, the deposition mount at the upstream and downstream side of the pipeline are predicted differently by different turbulence models. At the upstream side, using LES, Test 5 and Test 6 produce the bed profile with the best agreement with the measurements. Test 1 and Test 2 over-predicted slightly around $x = -2D$. The bed profile produced by $k - \omega$ model in Test 3 and Test 4 are worse than the results in tests either with LES or without turbulence model. With the $k - \omega$ model, the maximum amount of over-prediction in bed elevation is near $x = -2D$. In the downstream side, the bed elevation is over-predicted between $x = 2D$ and $x = 5D$. Results in Test 1 and Test 6 reach the best agreement with the measurement, while the results produced by $k-\omega$ model without modified viscosity in Test 3 see the biggest deviation from measurements. With respect to the effect of the modified viscosity, we can see that in each panel, tests with modified viscosity produce smoother bed profile at both the upstream and downstream side of the pipeline, which are closer to the measurements. Especially at the downstream side, the over-predicted bed elevation is reduced by adopting the modified viscosity. Therefore, the modified viscosity plays an important role in the interaction between the solid phase and the fluid phase, and consequently, it influences the formation of bed profile.

In Figure 12, the flow velocity vectors are plotted at every 50 points on the Eulerian grid. The flow pattern in Figure 12-a and Figure 12-b resemble each other, where the only difference between these two tests is whether the fluid viscosity is modified or not. Only the flow velocity very close to the bed surface is slightly different to each other. This finding also applies to the middle and bottom panels (see Figure 12-c, Figure 12-d, Figure 12-e and Figure 12-f). This is because the modified viscosity only influences the bed region, especially the regions of high solid volume fraction, and has little effect in the

main flow body as shown in Figure 10. However, the flow pattern produced with different turbulence models are different to each other. The detailed flow vector field plotted at every point on the Eulerian grid in Test 2, Test 4 and Test 6 are shown in Figure 13, in which no turbulence model, the standard $k-\omega$ turbulence model and LES is employed respectively. The acceleration jet beneath the pipeline in the scour hole, and the flow acceleration above the pipeline are all captured in these three tests. This serves as a prerequisite to the well captured scour hole in these tests. However, at the upstream side, only LES resolves the detailed vortices right above the bed surface (see Figure 13-c), while without turbulence modeling, only a small vortex is formed at $x = -2D$ (see Figure 13-b); and $k-\omega$ model generates a much bigger vortex in front of the upstream mount (see Figure 13-c), which explains the over-predicted bed elevation observed in Test 2 and Test 4. At the downstream side, without turbulence modeling, the recirculation zone behind the pipeline is bigger, and the dissipation of the vortex is much weaker than that modeled with LES. In test 4 with the $k-\omega$ model, the flow field at the downstream side is much distorted, and the weak flow region above the bed starting from $x = 2D$ and extending downstream is larger than that in the other two tests. Test 6 with LES resolves the fine details of the flow structure, and consequently, the predicted bed profile is in better agreement with the measurement.

4. Conclusions

In this paper, an Euler-Lagrange multiphase approach is employed to develop a new model for local scour and sand transport. The model is able to simulate a mobile bed with the free surface effect. The fluid phase is resolved on an Eulerian grid by solving the modified Navier-Stokes equations with a two-fluid methodology incorporating the Volume

of Fluid method for the free surface. The momentum transfer from the solid phase to the fluid phase is considered in the momentum equation. Particles' influence on the fluid viscosity is also reflected. The multiphase particle-in-cell method is adopted to solve the solid phase in a Lagrangian framework following Newton's Law of Motion. Therefore, the discrete-particle nature of the solid phase is very well represented. The movement of individual particles can be physically tracked at each time step, which reveals detailed sand transport and scour processes which continuum models struggle to achieve. The hydrodynamic drag force, pressure gradient force, net buoyancy force and inter-particle stress are all taken into account. Therefore, in this Euler-Lagrange scour model, the flow-particle coupling and particle-particle interactions are fully resolved, thus four-way coupling is achieved.

The model is calibrated via particle falling tests and isolated block tests. Then the model is applied to a benchmark scour case: current-induced live-bed scour around a pipeline. One of the advantages of this model is to resolve the sand transport in a natural way, therefore, the particle distribution and evolvement can be analyzed easily. The modeling results show that the scour development at the beginning is largely dominated by scattering events. The model is able to resolve the tunnel erosion stage well even with an initially flat bed. The effect of the modified viscosity mainly stabilizes the bed, and has little effect elsewhere.

LES and $k-\omega$ turbulence models are employed respectively to investigate the influence of hydrodynamics on the bed profile. The resolved flow field and bed profile are analyzed in details. It is found that LES can resolve the detailed vortex structures in the upstream side of the pipeline and the organized lee-wake vortices better than $k-\omega$ model. Consequently

659 the bed profile reproduced with LES is in better agreement with the measurements. It is
660 also found that the particle distribution overlaps with high value regions of sub-grid-scale
661 kinetic energy and sub-grid-scale eddy viscosity. The implication of the particle motion
662 with respect to the sub-grid-scale turbulence properties is supposed to play a part in sand
663 transport and scour process.

664 In short, an Euler-Lagrange multiphase approach is capable of resolving the sand trans-
665 port and scour process in a natural way. The scour prediction is satisfactory and the
666 mechanics involved in these processes is reflected.

667 **Acknowledgments.**

668 The authors would like to thank Engineering and Physical Sciences Research Council
669 (EPSRC) and HR Wallingford for their generous funding to this research.

References

670 A., Y. (1993), Bridging between eddy-viscosity-type and second-order turbulence models
671 through a two-scale turbulence theory, *Phys Rev E Stat Phys Plasmas Fluids Relat*
672 *Interdiscip Topics*, *48*(1), 273–281.

673 Andrews, M., and P. O'Rourke (1996), The multiphase particle-in-cell (mp-pic) method
674 for dense particulate flows, *International Journal of Multiphase Flow*, *22*(2), 379 – 402.

675 Eilers, H. (1941), The viscosity of the emulsion of highly viscous substances as function
676 of concentration, *Kolloid-Zeitschrift*, *97*(3), 313–321.

677 Einstein, A. (1906), Eine neue bestimmung der molekuldimensionen (german) [a new
678 determination of molecular dimensions], *Annalen der Physik*, *19*, 289C306.

679 Hirt, C., and B. Nichols (1981), Volume of fluid (vof) method for the dynamics of free
680 boundaries, *Journal of Computational Physics*, *39*(1), 201 – 225.
681 Issa, R. I. (1986), Solution of the implicitly discretised fluid flow equations by operator-
682 splitting., *Journal of Computational Physics*, *62*, 40–65.
683 Jasak, H. (1996), Error analysis and estimation for the finite volume method with appli-
684 cations to fluid flows, Ph.D. thesis, Imperial College, University of London.
685 Karimipour, S., and T. Pugsley (2012), Application of the particle in cell approach for the
686 simulation of bubbling fluidized beds of geldart a particles, *Powder Technology*, *220*(0),
687 63 – 69, selected Papers from the 2010 {NETL} Multiphase Flow Workshop.
688 Li, F., and L. Cheng (1999), A numerical model for local scour under offshore pipelines.,
689 *J Hydr Eng*, *125*, 400–406.
690 Li, F., and L. Cheng (2000), Numerical simulation of pipeline local scour with lee-wake
691 effects., *Int J Offshore Polar Eng*, *10*, 195–199.
692 Liang, D., L. Cheng, and K. Yeow (2005), Numerical study of the reynolds-number de-
693 pendence of two-dimensional scour beneath offshore pipelines in steady currents, *Ocean*
694 *Engineering*, *32*(13), 1590 – 1607.
695 Macpherson, N. N., G.B., and H. Weller (2009), Particle tracking in unstructured, ar-
696 bitrary polyhedral meshes for use in cfd and molecular dynamics, *Commun. Numer.*
697 *Meth. Engng*, *25*, 263–273.
698 Mao, Y. (1986), *The Interaction Between a Pipeline and an Erodible Bed*, Institute of
699 Hydrodynamics and Hydraulic Engineering København: Series paper, Institute of Hy-
700 drodynamics and Hydraulic Engineering, Technical University of Denmark.

Nordin, N. (2000), Complex chemistry modemodel of diesel spray combustion., Ph.D. thesis, Chalmers University of Technology, Gothenburg.

Patankar, N., and D. Joseph (2001), Lagrangian numerical simulation of particulate flows, *International Journal of Multiphase Flow*, *27*(10), 1685–1706.

Patankar, S. (1981), *Numerical heat transfer and fluid flow*, Hemisphere Publishing Corporation.

Penko, A., J. Calantoni, and D. Slinn (2009), Mixture theory model sensitivity to effective viscosity in simulations of sandy bedform dynamics, in *OCEANS 2009, MTS/IEEE Biloxi - Marine Technology for Our Future: Global and Local Challenges*, pp. 1–9.

Prendergast, L., K. Gavin, and P. Doherty (2015), An investigation into the effect of scour on the natural frequency of an offshore wind turbine, *Ocean Engineering*, *101*(0), 1 – 11.

Rusche, H. (2002), Computational fluid dynamics of dispersed two-phase flows at high phase fractions, Ph.D. thesis, Imperial College, University of London.

Snider, D. (2001), An incompressible three-dimensional multiphase particle-in-cell model for dense particle flows, *Journal of Computational Physics*, *170*(2), 523–549.

Snider, D., P. O'Rourke, and M. Andrews (1998), Sediment flow in inclined vessels calculated using a multiphase particle-in-cell model for dense particle flows, *International Journal of Multiphase Flow*, *24*(8), 1359 – 1382.

Solnordal, C. B., V. Kenche, T. D. Hadley, Y. Feng, P. J. Witt, and K.-S. Lim (2015), Simulation of an internally circulating fluidized bed using a multiphase particle-in-cell method, *Powder Technology*, *274*(0), 123 – 134.

Sumer, B., and J. Fredsøe (2002), *The Mechanics of Scour in the Marine Environment*, Advanced Series on Ocean Engineering, World Scientific.

van Rijn, L. (1993), *Principles of sediment transport in rivers, estuaries and coastal seas*, Principles of Sediment Transport in Rivers, Estuaries, and Coastal Seas, Aqua Publications.

Whitehouse, R. J., J. M. Harris, J. Sutherland, and J. Rees (2011), The nature of scour development and scour protection at offshore windfarm foundations, *Marine Pollution Bulletin*, *62*(1), 73 – 88.

Yeganeh-Bakhtiary, A., M. H. Kazeminezhad, A. Etemad-Shahidi, J. H. Baas, and L. Cheng (2011), Euler-euler two-phase flow simulation of tunnel erosion beneath marine pipelines, *Applied Ocean Research*, *33*(2), 137 – 146.

Yeganeh-Bakhtiary, A., M. Zanganeh, E. Kazemi, L. Cheng, and A. W. AK. (2013), Eulerclagrange two-phase model for simulating live-bed scour beneath marine pipelines., *ASME. J. Offshore Mech. Arct. Eng.*, *135*(3).

Zanganeh, M., A. Yeganeh-Bakhtiary, and A. K. A. Wahab (2012), Lagrangian coupling two-phase flow model to simulate current-induced scour beneath marine pipelines, *Applied Ocean Research*, *38*(0), 64 – 73.

Zhao, Z., and H. Fernando (2007), Numerical simulation of scour around pipelines using an euler-euler coupled two-phase model, *Environmental Fluid Mechanics*, *7*, 121–142.

Zhu, H., X. Qi, P. Lin, and Y. Yang (2013), Numerical simulation of flow around a submarine pipe with a spoiler and current-induced scour beneath the pipe, *Applied Ocean Research*, *41*(0), 87 – 100.

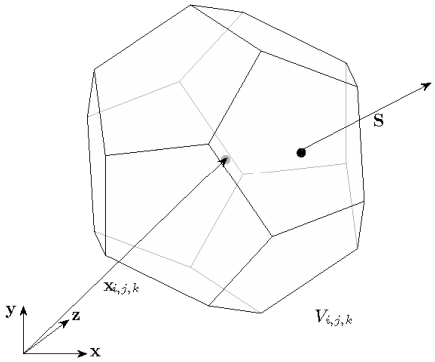

Figure 1. Control volume.

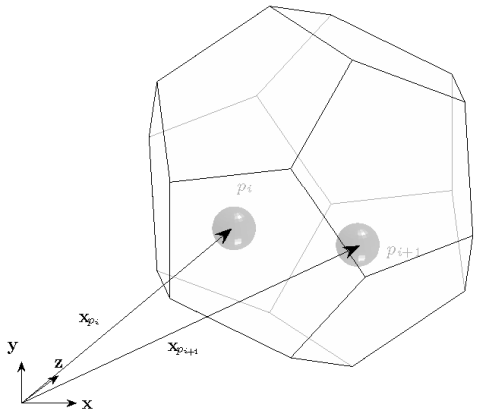

Figure 2. Sketch of particles within a control volume.

Table 1. Particle properties in Test PFV-1 and PFV-2

Test number	Number of particles per parcel	Particle d_{50}
PFV-1	1	2.5 mm
PFV-2	1000	0.25 mm

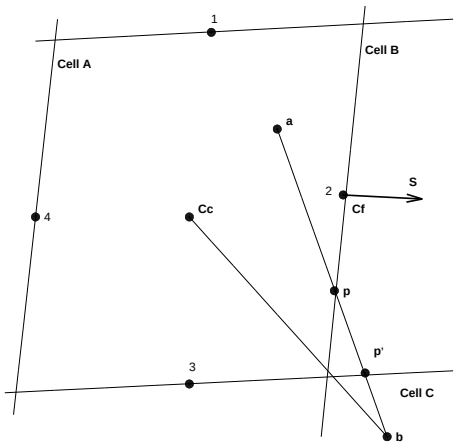

Figure 3. Sketch of a particle moving from original position **a** to final position **b**. After *Macpherson and Weller* [2009]

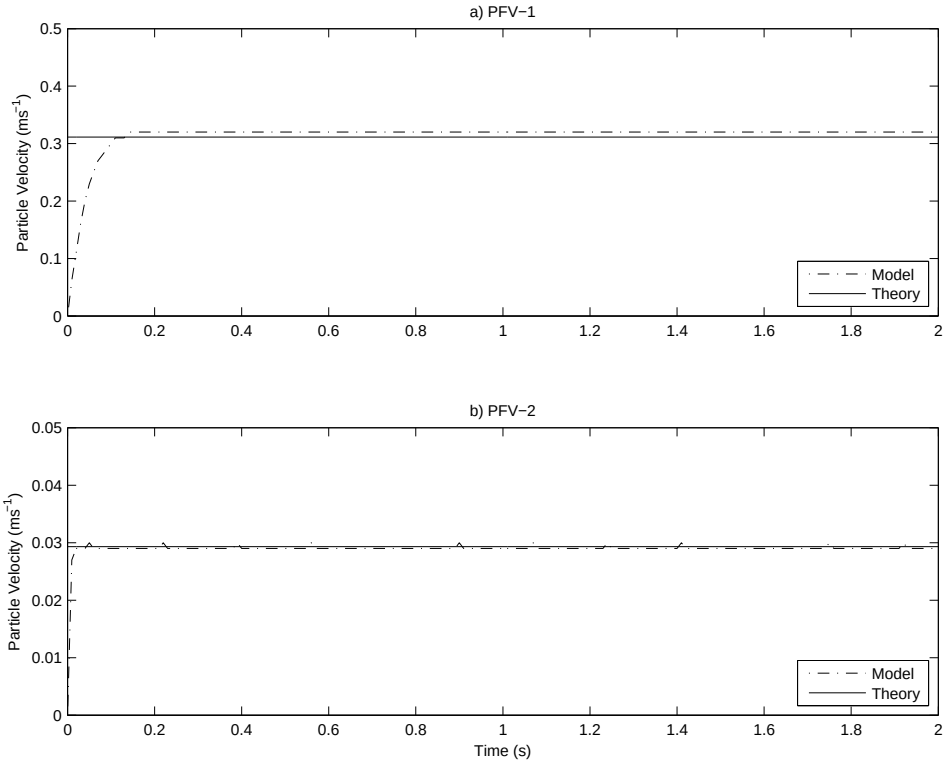

Figure 4. Modeled particle fall velocities in comparison with the theoretical values.

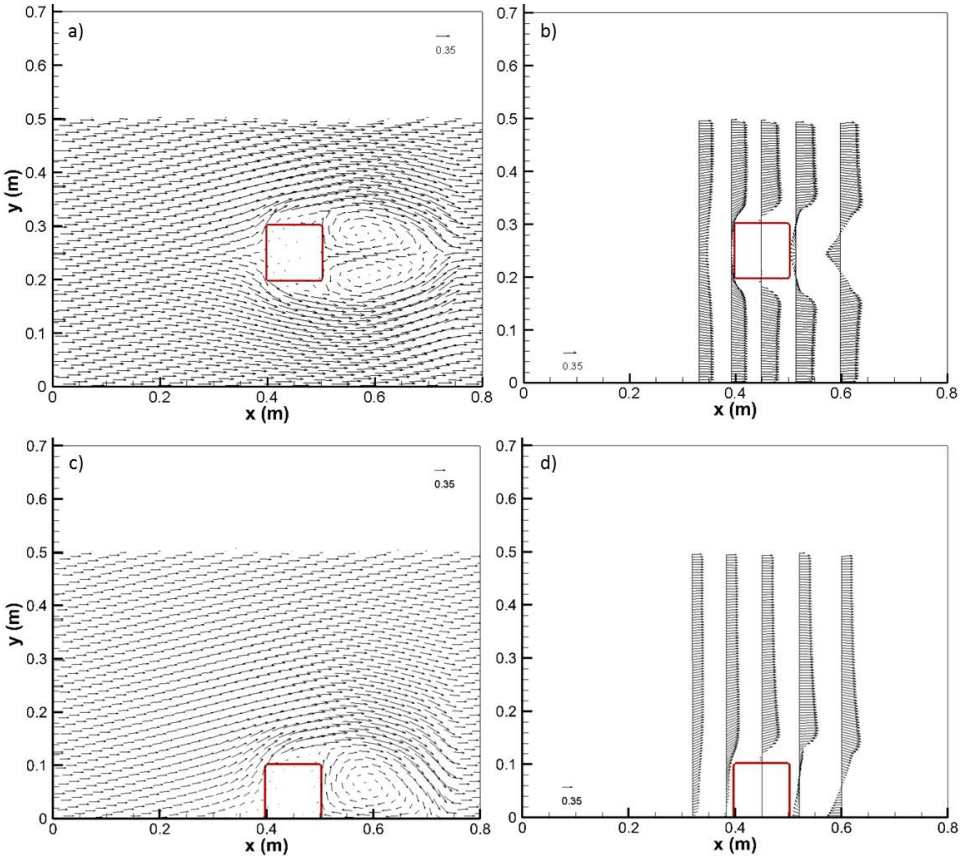

Figure 5. Velocity vector field (left column) and velocity vector profiles at selected sections (right column) in Tests MDL (top panel), BTM (middle panel), and CRN (bottom panel). Red Line: the boundary of the block.

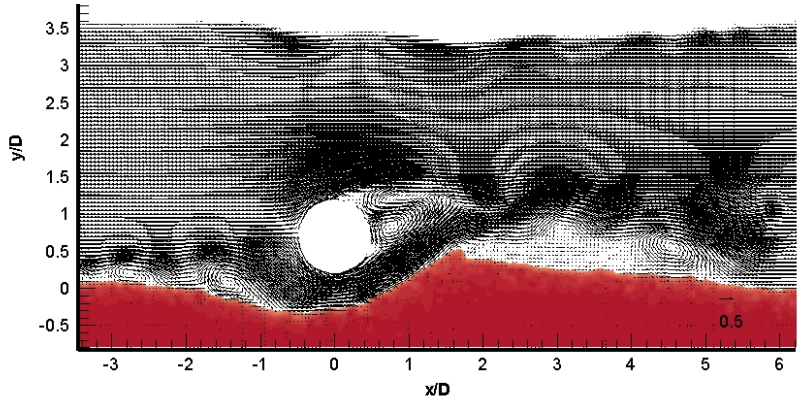

Figure 6. Modeled flow velocity field at $t = 1.5\ min$.

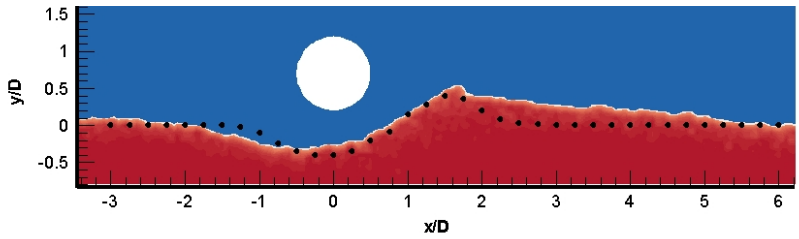

Figure 7. Modeled bed profile at $t = 1.5\ min$ in comparison with the measurements (black dots).

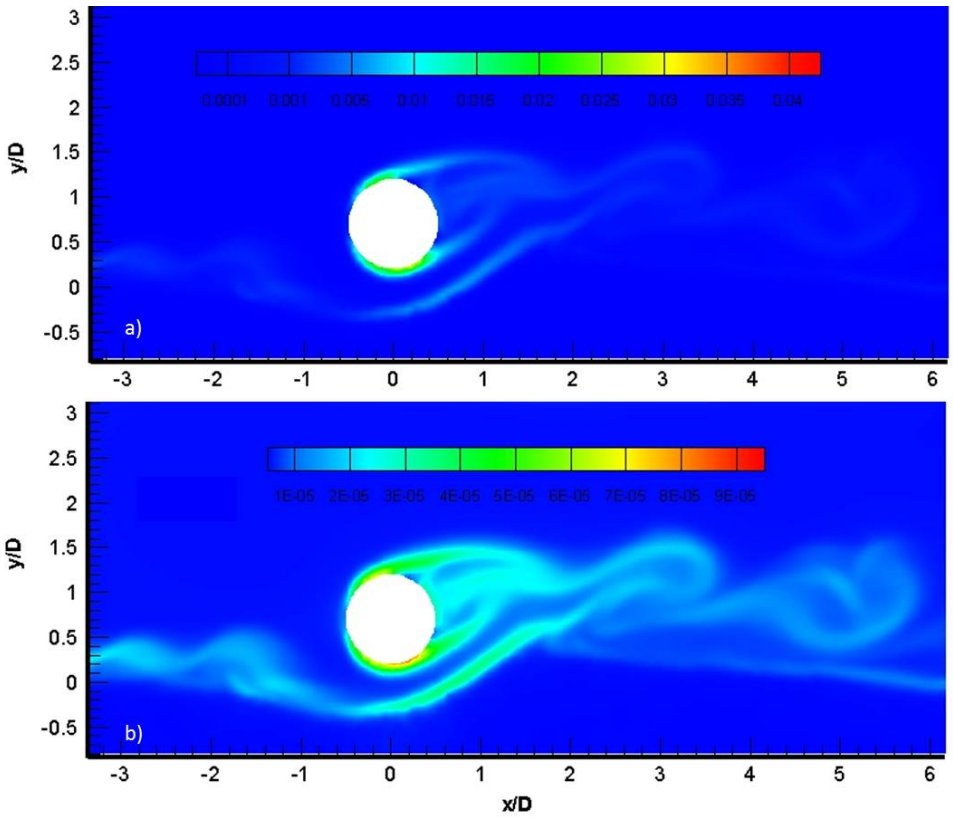

Figure 8. Contour of sub-grid-scale kinetic energy (a) and sub-grid-scale eddy viscosity (b) at $t = 1.5\ min$.

Table 2. Tests set-up for the pipeline scour case.

Test number	Modified fluid viscosity	$k-\omega$ turbulence model	LES modeling
1	○	○	○
2	√	○	○
3	○	√	○
4	√	√	○
5	○	○	√
6	√	○	√

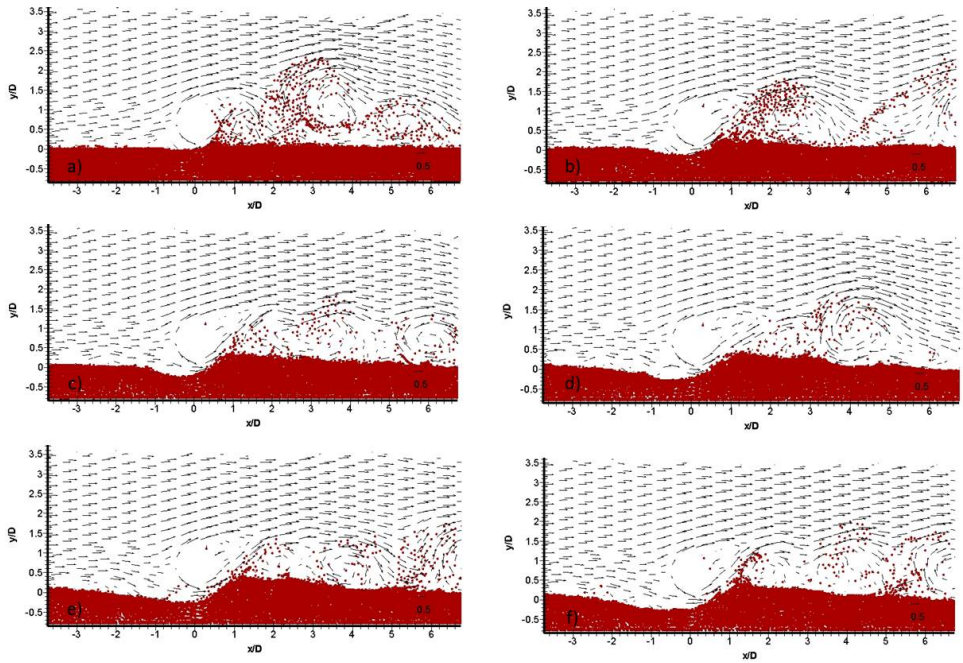

Figure 9. Particle distribution at selected time. *a*) $t = 4$ *s*, *b*) $t = 12$ *s*, *c*) $t = 24$ *s*, *d*) $t = 37$ *s*, *e*) $t = 41$ *s*, *f*) $t = 45$ *s*.

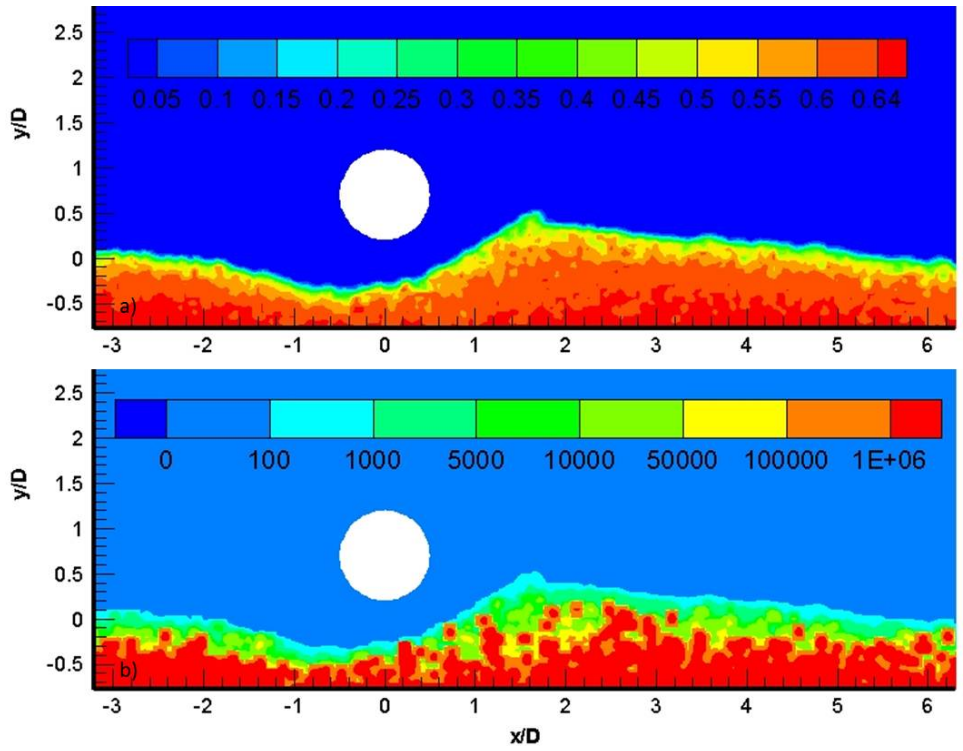

Figure 10. Contour of solid volume fraction (a) and modified viscosity (b) at $t = 1.5$ *min*.

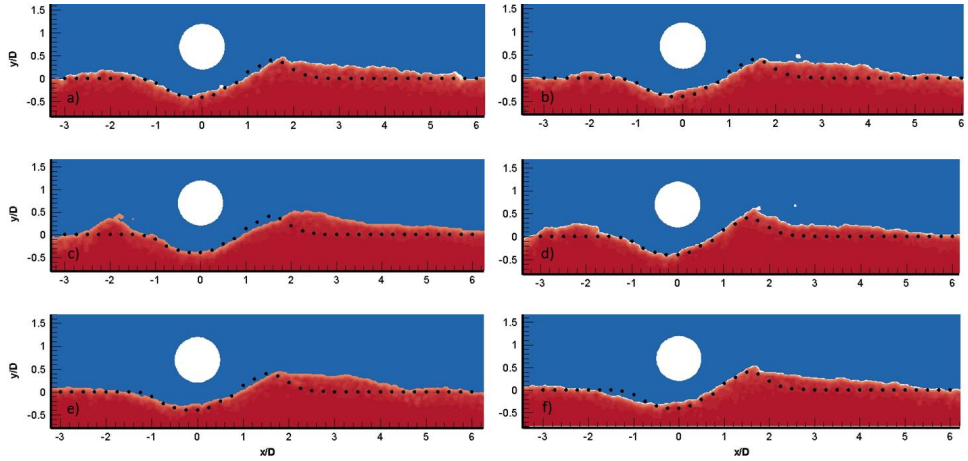

Figure 11. Modeled bed profile at $t = 1.5\ min$ in comparison with the measurements (black dots). From a) to f) are Test 1 to Test 6 in sequence.

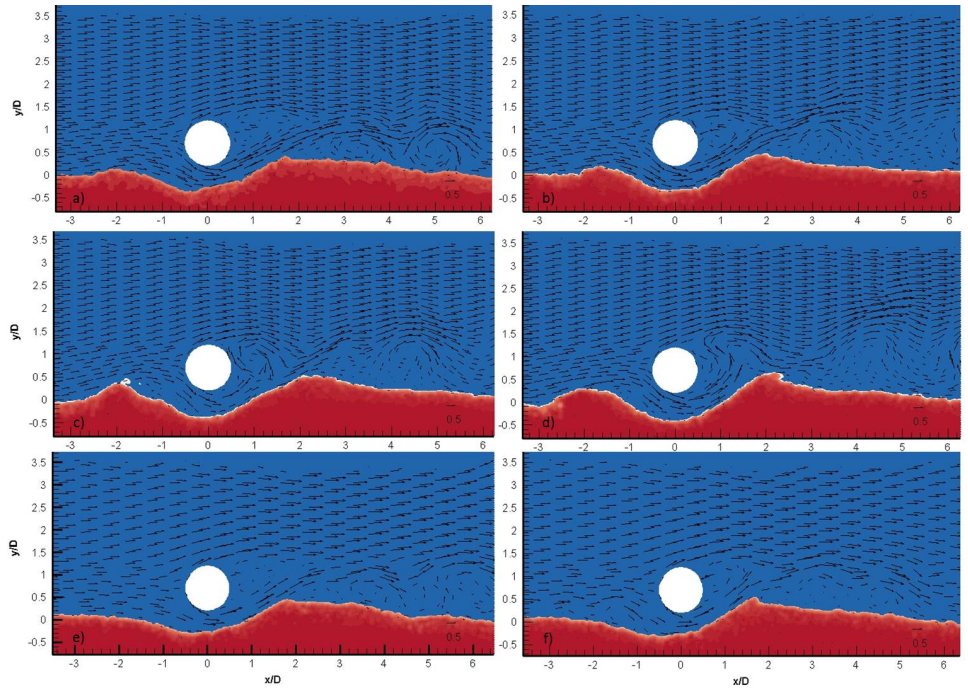

Figure 12. Modeled flow velocity field at $t = 1.5\ min$. From a) to f) are Test 1 to Test 6 in sequence.

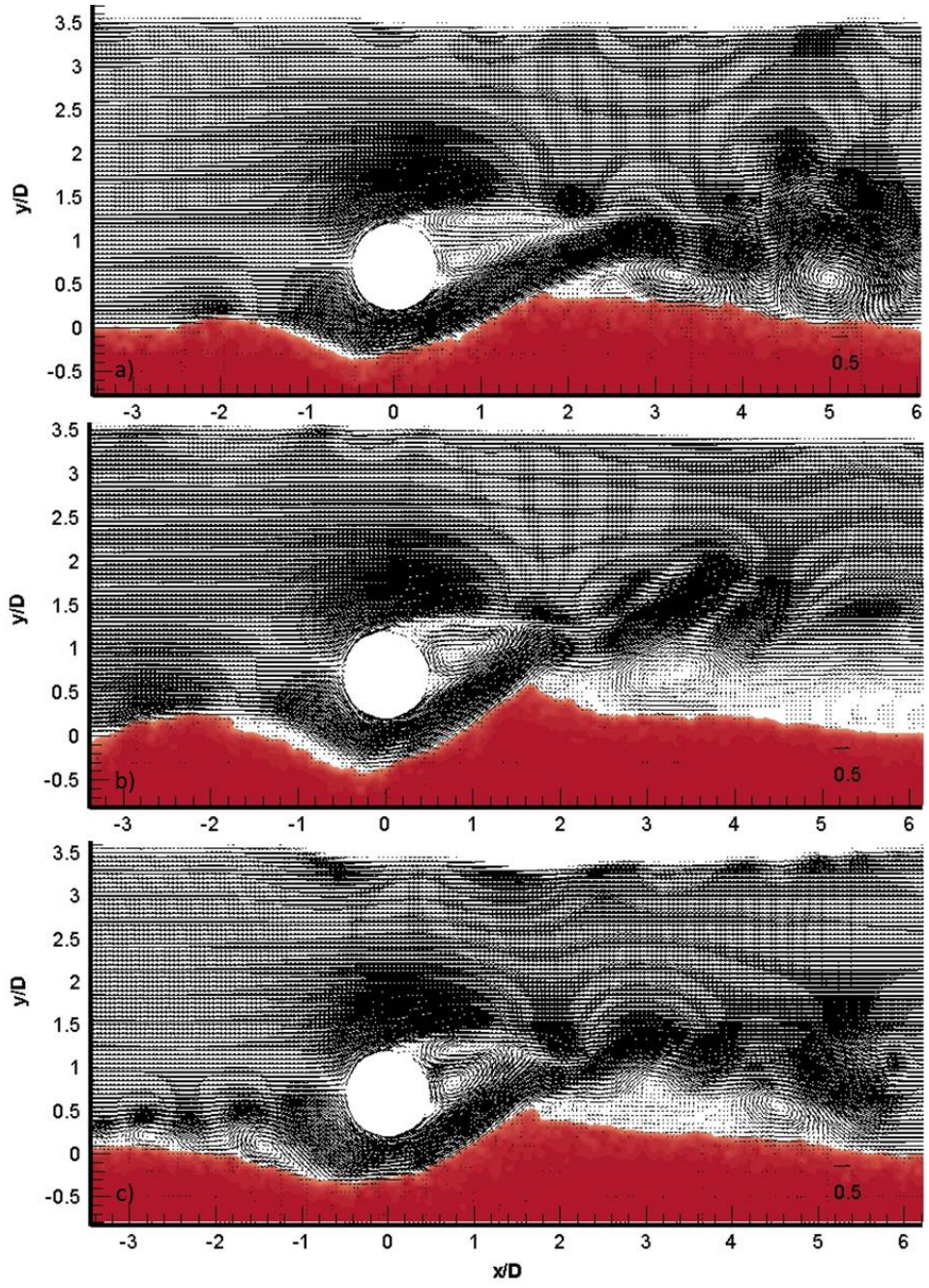

Figure 13. Detailed flow velocity field at $t = 1.5\ min$ in Test 2 (a), Test 4 (b), and Test 6 (c).